

## Article

# Wear Regularity of Shotcrete Conveying Bend Based on CFD-DEM Simulation

Yujie Hou <sup>1</sup>, Siyuan Song <sup>1</sup>, Jiahao Sun <sup>1</sup>, Guoming Liu <sup>1,\*</sup>, Jianguo Liu <sup>2,3,\*</sup> , Xiangfei Cui <sup>1</sup> and Qianqian Xu <sup>1</sup>

<sup>1</sup> College of Safety and Environmental Engineering, Shandong University of Science and Technology, Qingdao 266590, China

<sup>2</sup> NHC Key Laboratory for Engineering Control of Dust Hazard, Beijing 100000, China

<sup>3</sup> School of Civil and Resource Engineering, University of Science and Technology Beijing, Beijing 100083, China

\* Correspondence: skd995978@sust.edu.cn (G.L.); liujg@ustb.edu.cn (J.L.)

**Abstract:** To reveal the flow characteristics of shotcrete during pneumatic transportation, the numerical simulation of the gas–solid flow of shotcrete in the pipeline transportation process was carried out based on a CFD-DEM coupling simulation method. When the particle diameter increased from 7 mm to 12 mm, the maximum wear depth of the pipeline increased from  $1.48 \times 10^{-6}$  mm to  $4.58 \times 10^{-6}$  mm. With an increase in particle diameter, the maximum wear depth of the pipeline increased. Moreover, the wear position gradually concentrated to a fixed area with the increase in particle diameter. In the wind speed range of this simulation study, when the wind speed increased from 42 m/s to 52 m/s, the maximum wear depth of the pipeline increased from  $2.53 \times 10^{-6}$  mm to  $5.26 \times 10^{-6}$  mm. The change in wind speed had little effect on the wear location of the pipeline. However, the wear depth of the pipeline increased with the increase in wind speed. When the curvature radius increased from 200 mm to 250 mm, the maximum wear depth decreased from  $5.83 \times 10^{-6}$  mm to  $4.47 \times 10^{-6}$  mm. When the curvature radius increased to 300 mm, the maximum wear depth increased to  $6.58 \times 10^{-6}$  mm. Finally, according to the law of pipeline wear and combined with the actual situation of pipeline wear in engineering, measures were put forward to prevent or reduce the degree of pipeline wear.

**Keywords:** shotcrete; pneumatic conveying; pipeline wear; two-phase flow; numerical simulation



**Citation:** Hou, Y.; Song, S.; Sun, J.; Liu, G.; Liu, J.; Cui, X.; Xu, Q. Wear Regularity of Shotcrete Conveying Bend Based on CFD-DEM Simulation. *Buildings* **2023**, *13*, 415. <https://doi.org/10.3390/buildings13020415>

Academic Editors: Ahmed Senouci and Elena Ferretti

Received: 24 December 2022

Revised: 29 January 2023

Accepted: 31 January 2023

Published: 2 February 2023



**Copyright:** © 2023 by the authors. Licensee MDPI, Basel, Switzerland. This article is an open access article distributed under the terms and conditions of the Creative Commons Attribution (CC BY) license (<https://creativecommons.org/licenses/by/4.0/>).

## 1. Introduction

In recent years, shotcrete technology has been widely used in underground engineering, geotechnical engineering and municipal engineering [1]. The concrete spraying process mainly relies on pneumatic conveying. The problem of pipe wear during pneumatic conveying is common and difficult to avoid. Wear is a common loss phenomenon in industry, with about 80% of machinery parts failing due to wear and tear. According to statistics, the loss of erosive wear has been estimated to range from 1% to 4% of the gross national product of an industrialized country [2]. In the process of conveying shotcrete material, there are many solid particles such as sand and gravel in the pipeline. In general, high pressure air is the power source of particle transportation in the pipe when spraying concrete. The wet or semi-wet concrete particles are carried by high pressure air through the pipeline and then sprayed on the wall. Solid particles are likely to cause severe collision and friction with the inner wall of the pipeline, resulting in pipe wear [3–5]. Moreover, in pipeline transportation, bent pipes are more prone to wear than straight pipes [6,7]. If the pipeline is worn, the service life of the pipeline will be reduced and the maintenance cost will be increased. Moreover, energy consumption will increase. If part of the wear is serious, an eddy current will also be generated. The material will not be evenly distributed in the pipeline section, affecting the efficiency of material transportation. If pipes are worn through and materials leak, environmental pollution and safety accidents may occur. Therefore, it is of great significance to study the law of pipeline wear in shotcrete technology and put forward

control measures, which can effectively reduce construction costs and energy consumption, prolong the service life of pipelines and prevent safety accidents [8].

In the early stages, some scholars achieved some theoretical results on erosion wear through experimental methods. However, the erosion wear experiments had some shortcomings with long cycles, complex processes, high experimental costs and a lack of predictability [9,10]. Erosion wear experimentation was gradually abandoned by researchers. With the development of science and technology, the development of numerical simulation software is gradually maturing. The study of wear is beginning to adopt the numerical simulation method [11–13]. Many scholars have carried out research on erosion wear with the numerical simulation method for typical pipe structures such as elbow pipes and tee pipes. Bitter [14] studied the theory of deformation wear. The erosion wear was divided into deformation wear and cutting wear, and the total amount of wear was equal to the deformation wear plus the cutting wear. Tilly [15] examined the theory of secondary erosion wear and divided the erosion process into two stages: the primary erosion caused by the direct incidence of particles and the secondary erosion caused by particle breakage. Zhang et al. [16] proposed the theory of micro-cutting wear, investigating the relationship between the erosion rate and impact angle and impact velocity. Hutchings [17] created a material erosion model under continuous impact by particles. This model achieved high calculation accuracy under the impact angle of  $90^\circ$ , but it performed poorly under the rest of the impact angles. The University of Tulsa has refined the empirical model established by Ahlert to predict the wear rate of AISI1018 steel, known as the ‘Tulsa model’, which can be used to predict the wear rates of bends, tees and reducers [18].

Chen et al. [19] combined the random rebound model with the Tulsa model and applied it to analyze the wear degree of elbows and tees based on CFD. Ding et al. [20] analyzed the erosion wear of a right-angle bend pipe using the Tulsa model. The most serious erosion position of the right-angle bend pipe was found to analyze the influence of flow velocity, particle concentration and particle diameter on the erosion rate. Liu et al. [21] investigated the wear of catalyst particles at 90-degree elbows during hydraulic transport by coupled CFD-DEM. The authors analyzed the effects of the particle model shape, radius of curvature and bending angle on the wear characteristics of liquid–solid two-phase flow. Tan et al. [22] verified the effectiveness of the coupling model by taking pneumatic conveying as an example. The collision frequency of particles against the elbow was monitored by simulating the shotcrete pumping process. A new time-average collision strength model based on impact force was proposed to study the wear mechanism of the elbow. The location of the maximum erosion wear damage of the elbow was predicted. Wang et al. [23] investigated the mechanism of charging slurry pipe wear by developing a pipe wear loop test system to test different cement-to-tailings ratios, high concentrations and flow rates.

The factors affecting pipeline wear are mainly divided into three categories: the nature of the conveying materials, the nature of the pipelines and the conveying conditions. Many scholars have studied the factors affecting pipeline wear through numerical simulation. Chen et al. [24] used CFD-DEM coupling numerical simulation to predict the main wear position of a shotcrete-conveying pipeline and mainly studied the influence of different gas velocities and feed rates on the wear volume of the pipeline. Singh et al. [25] evaluated the  $k-\epsilon$  turbulence model and the mixture model to conduct simulation research and analyzed the effects of different fluid velocities, bend radii of curvature, pipeline diameters and particle sizes on pipeline wear. Wang et al. [26] took reducing elbow pipes with different structures as their research object and established a flow model of a slurry in reducing elbow pipes by using Fluent to study the erosion wear law of filling a slurry in reducing pipes. Naveh et al. [27] examined the mechanism of slurry pipeline wear by studying the form of solid particle movement in the slurry. The influence of the slurry flow rate played a key role on the pipeline wear. Li et al. [28] studied the influence of slurry velocity on pipeline wear under different cement–sand ratios and different mass concentrations of filling slurry based on an ANSYS three-dimensional numerical calculation model. Zhou

et al. [29] used Fluent software to simulate the wear of horizontal conveying pipes. The authors focused on the effect of solid particle concentration on the degree of wear. Sun et al. [30] conducted numerical simulation on the erosion wear of bends based on the coupled CFD-DEM method and SIEM, which were verified by relevant experimental data. Wang et al. [31] applied the DPM erosion model to study the wear of pipes in refrigeration systems. The wear condition of impurity particles on the pipe wall was investigated under different gas velocity and solid phase concentration conditions.

The use of reasonable measures can effectively reduce the degree of pipe wear. Many scholars have proposed preventive measures for pipe wear. Ma et al. [32] studied the two-phase flow motion characteristics of concrete in pipes based on a CFD-DEM coupling model and field measurement. The particle velocity exhibited minimal loss at a bend angle of 90 degrees which provided a guidance in the pipeline wear field. Liu et al. [33] investigated the protective effect of diamond-like carbon film on pipes through hollow cathode plasma-enhanced chemical vapor deposition (HC-PECVD) technology, which effectively prevented the corrosion and wear of the inner surface of the pipes. Guo et al. [34] proposed three types of elbow structures with circumferentially distributed bionic transverse grooves, bionic ribs and a single rib on the inner wall to improve the anti-erosion characteristics of the elbows. Zhou et al. [35] analyzed the effects of air velocity and air pressure on elbow erosion. The pressure drop was studied by an orthogonal design and the best parameters of elbow pneumatic conveying were summarized. Li et al. [36] used the CFD-DEM coupling method to simulate the transportation process of large-particle coal and found that the concentration of coal particles in the central area was beneficial to reducing pipeline wear.

In summary, many scholars at home and abroad have conducted in-depth research on the wear of grain-conveying pipes, dredging pipes, ash-conveying pipes, natural gas pipelines, etc. They have also put forward corresponding preventive measures. However, the research on the wear of shotcrete particle pneumatic conveying pipes is still relatively scarce, so this paper mainly focuses on the wear law of shotcrete pneumatic conveying pipes and puts forward corresponding preventive or control measures according to the wear law and the wear situation in actual projects.

## 2. Theoretical Model

Fluent is a hydrodynamic simulation software, within which the Eulerian–Lagrangian model was selected for simulation. The realizable  $k$ - $\varepsilon$  model was chosen to reflect airflow migration behaviors. The Archard wear model was used to calculate the wear depth of the material surface. The shotcrete particles were regarded as discrete phase. In general, when the volume fraction of the discrete phase in the continuous phase was less than 10%, the discrete phase model (DPM) in Lagrangian coordinates was adopted to simulate the discrete phase and obtain the motion trajectory in the airflow field [37,38].

### 2.1. Airflow Motion Control Equation

#### (1) Quality control equation

The quality control equation was a continuity equation. In the numerical simulations, the fluid was considered as a continuity medium and followed the continuity equation [39]:

$$\frac{\partial(\varepsilon\rho)}{\partial t} + \nabla \cdot (\rho\varepsilon v) = 0 \quad (1)$$

where  $\rho$  is the gas density,  $\text{kg}/\text{m}^3$ ;  $t$  is the time,  $s$ ;  $\nabla$  denotes the Hamiltonian differential operators;  $\varepsilon$  denotes the volume fraction of the gas term; and  $v$  is the gas velocity,  $\text{m}/\text{s}$ .

#### (2) Momentum control equation

All fluid flows are subject to the momentum control equation [40]:

$$\frac{\partial(\varepsilon\rho)}{\partial t} \nabla (\rho\varepsilon v^2) = -\nabla P + \nabla(\mu\varepsilon\nabla v) + \rho\varepsilon g - S \quad (2)$$

where  $\rho$  is the gas density,  $\text{kg}/\text{m}^3$ ;  $v$  is the velocity of gas,  $\text{m}/\text{s}$ ;  $P$  is the pressure on gas microelements,  $\text{N}$ ;  $\mu$  is the gas dynamic viscosity,  $\text{Pa}\cdot\text{s}$ ;  $g$  is the gravitational acceleration,  $\text{m}/\text{s}^2$ ; and  $S$  indicates the momentum source term.

### (3) Turbulence model

The fluid motion in the simulation was expressed in the form of turbulence. The standard  $k$ - $\varepsilon$  model could satisfy most of the fluids with good computational accuracy [41,42].

Turbulent kinetic energy transport equation:

$$\frac{\partial}{\partial t}(\rho k) + \frac{\partial}{\partial x_i}(\rho k u_i) = \frac{\partial}{\partial x_j} \left[ \left( \mu + \frac{\mu_i}{\sigma_k} \right) \frac{\partial k}{\partial x_j} \right] + G_k + G_b - \rho \varepsilon - Y_M + S_k \quad (3)$$

Turbulent kinetic energy dissipation rate:

$$\frac{\partial}{\partial t}(\rho k) + \frac{\partial}{\partial x_i}(\rho \varepsilon u_i) = \frac{\partial}{\partial x_j} \left[ \left( \mu + \frac{\mu_i}{\sigma_k} \right) \frac{\partial \varepsilon}{\partial x_j} \right] + C_{1\varepsilon} \frac{\varepsilon}{k} (G_k + G_{3\varepsilon} + G_b) - C_{2\varepsilon} \rho \frac{\varepsilon^2}{k} + S_\varepsilon \quad (4)$$

Turbulent viscosity:

$$\mu_t = \rho C_\mu \frac{k^2}{\varepsilon} \quad (5)$$

where  $G_k$  represents the turbulent kinetic energy from laminar velocity gradients;  $G_b$  is the turbulent kinetic energy generated by buoyancy; and  $Y_M$  refers to fluctuations arising from excessive diffusion in compressible turbulent flows.

## 2.2. Particle Flow Control Equation

The motion of a particle is expressed mainly through the relation between velocity and displacement, following Newton's second law [43]:

$$\begin{cases} m_i \ddot{u}_i = \sum F \\ I_i \ddot{\theta}_i = \sum M \end{cases} \quad (6)$$

where  $m_i$  is the mass of particle  $i$ ,  $\text{kg}$ ;  $\ddot{u}_i$  is the acceleration of particle  $i$ ,  $\text{m}/\text{s}^2$ ;  $I_i$  represents the rotational inertia of particle  $i$ ;  $\ddot{\theta}_i$  refers to the angular velocity of particle  $i$ ;  $\sum F$  is the combined external force on particle  $i$ ,  $\text{N}$ ; and  $\sum M$  is the combined external moment of particle  $i$ . When a particle is in motion, it is subject to its own forces, such as inertial forces and gravity:

$$F_i = \frac{\pi d_p^3}{6} \rho_p \frac{d\mu_p}{dt} \quad (7)$$

$$F_g = m_p g = \frac{1}{6} \pi d_p^3 \rho_p g \quad (8)$$

where  $d_p$  means the radius of particles,  $\text{m}$ ;  $\rho_p$  represents the density of particles,  $\text{kg}/\text{m}^3$ ;  $\mu_p$  refers to the velocity of particles,  $\text{m}/\text{s}$ ; and  $m_p$  is the particle quality,  $\text{kg}$ .

## 2.3. Wear Model

Hertz-Mindlin with Archard wear was chosen as the wear model in this simulation. The standard Hertz-Mindlin contact model was used to calculate the wear depth of the material surface. The Archard wear model shows that the greater the friction generated by particles on the surface of material, the greater the amount of material removed [44]:

$$Q = W F_n dt \quad (9)$$

where  $Q$  means the volume of material removed;  $F_n$  represents the normal force of the particle in contact with the wall;  $dt$  is the tangential sliding distance of particles along the

wall; and  $W$  refers to the initial wear constant. The wear constant for this simulation was taken as  $3.2 \times 10^{-14} \text{ pa}^{-1}$ .

The wear depth of each cell in EDEM is

$$dp = Q/A \quad (10)$$

where  $dp$  is the wear depth of each cell in EDEM and  $A$  means the contact area of particles with the wall.

### 3. Simulation Boundary Conditions

#### 3.1. Geometric Models

In pipeline transportation, the wear degree of the bend part was more serious, so this paper focused on the wear of the bend part. In this simulation, ICEM CFD was used to establish the geometric model of the pipeline (Figure 1). The pipeline model parameters were set as shown in Table 1.

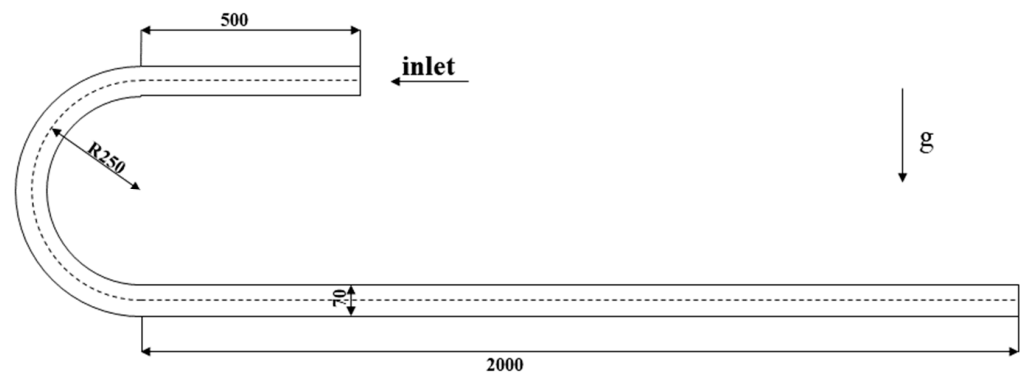


Figure 1. Geometric model of conveying pipeline.

Table 1. Pipeline model parameters.

Designation	Entrance Straight Pipe	Export Straight Pipe	Radius of Curvature	Pipe Diameter
Size	500 mm	2000 mm	200 mm, 250 mm, 300 mm	70 mm

#### 3.2. Parameter Settings

##### (1) EDEM parameter settings

The coarse aggregate is generally a particle with a diameter of 4.75–15 mm. To simplify the calculation, the coarse aggregate was considered as a single sized spherical particle. The parameters of the particles are shown in Table 2.

Table 2. Parameter settings for particles and conveying pipes.

	Density	Poisson's Ratio	Shear Modulus	Size
Coarse Aggregate	2300 kg/m <sup>3</sup>	0.3	$1 \times 10^8$	7 mm, 8 mm, 9 mm, 10 mm, 11 mm, 12 mm
Pipeline	7850 kg/m <sup>3</sup>	0.25	$8 \times 10^{10}$	As shown in Table 1

The particle-to-tube wall and particle-to-particle contact parameters are shown in Table 3.

##### (2) Fluent parameter settings

The air fluid phase was set to a density of 1.225 kg/m<sup>3</sup> and a kinetic viscosity of  $1.8 \times 10^{-5} \text{ kg}/(\text{m}\cdot\text{s})$ . The boundary conditions in Fluent are shown in Table 4.

**Table 3.** Contact parameters.

	Contact Model	Recovery Coefficient	Static Friction Coefficient	Rolling Friction Coefficient
Pellets–Pellets	Hertz-Mindlin with JKR	0.4	1	0.06
Granule–Tube wall	Hertz-Mindlin with Archard wear	0.5	0.5	0.2

**Table 4.** Boundary conditions.

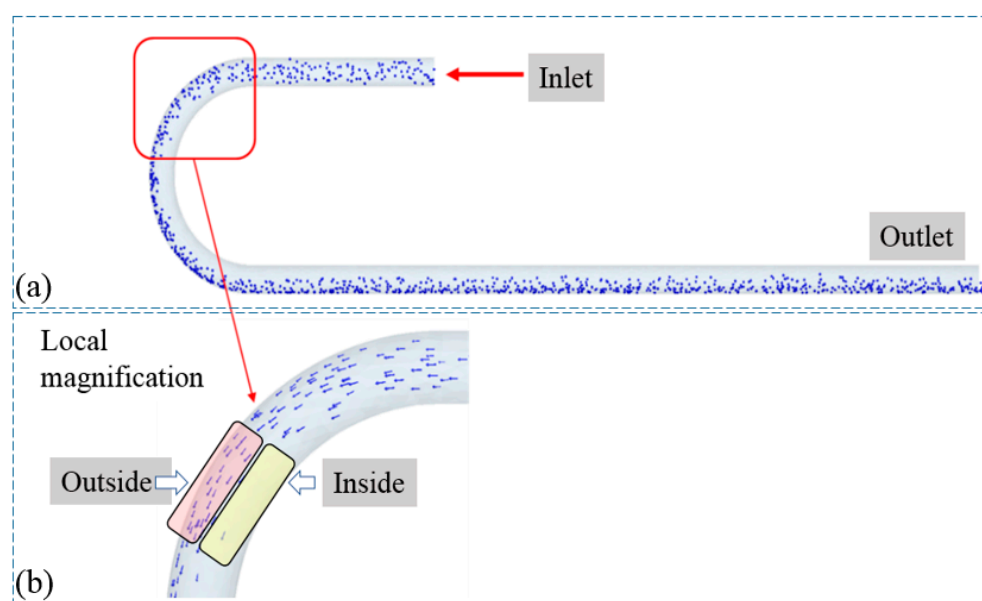
Type	Numerical Value	Turbulence Intensity	Hydraulic Diameter
Velocity inlet	42 m/s, 44 m/s, 46 m/s, 48 m/s, 50 m/s, 52 m/s	5%	70 mm
Pressure outlet	0.1 MPa	5%	70 mm

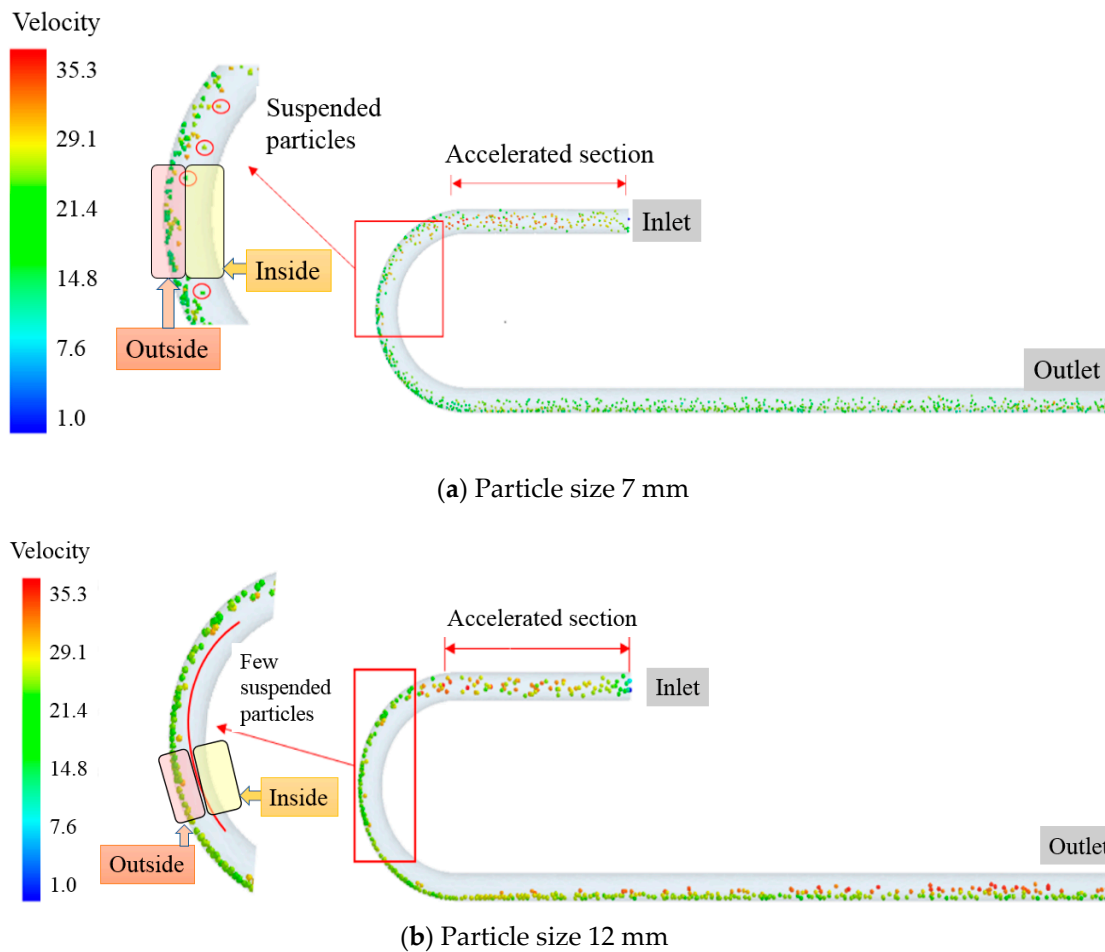
## 4. Results and Discussion

### 4.1. Particle Motion Analysis

The distribution characteristics of the particles are shown in Figures 2 and 3. The particles were blown up in suspension by compressed air in the inlet straight pipe. Particles moved forward under the action of air. Figure 2 mainly represents the movement process of the particles in the pipeline. In order to see the distribution of particles more clearly, Figure 2b is a partial enlargement of Figure 2a above it. More information is shown in Figure 3 which indicates the different states of large and small particles in the pipeline. When the particles reached the bend part, a large number of particles hit the wall and then slid along the outside of the pipe wall. After leaving the bend, the particles still accumulated at the bottom of the pipe due to inertia. They were suspended again in the pipe by the action of air until the outlet of the pipe.

The particles were gradually accelerated by the action of air after entering the inlet section. When the particles reached the bend part, a large number of particles hit the wall and the particle velocity dropped rapidly. However, the particle velocity did not decrease to a minimum value, but gradually decreased as the particles slid along the outside of the pipe. After leaving the bend, the particles were again suspended in the pipe until the outlet of the pipe.

**Figure 2.** Particle distribution in the (a) total pipeline and (b) partial enlargement of the bend.



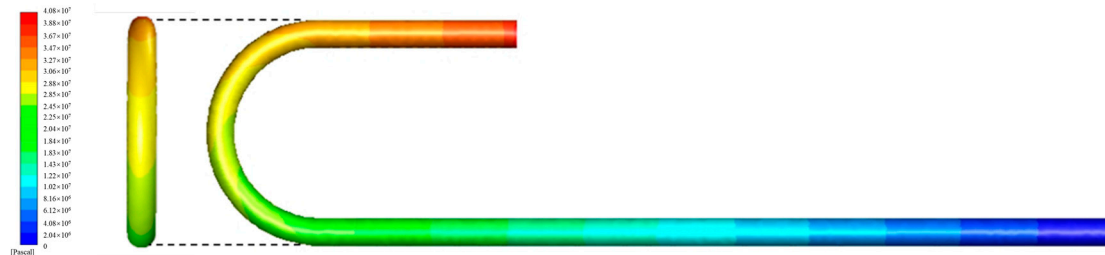
**Figure 3.** Velocity distribution of particles in the pipeline.

Figure 3a,b shows the particle distribution for particle sizes of 7 mm and 12 mm, respectively. When the particle size was 7 mm, the mass of the particle was smaller and its own inertial force was smaller. The compressed air had a stronger role in carrying the particle. When the particles passed through the bend, some of the particles moved in the direction of the airflow. So, the particles of 7 mm in diameter passing through the bend were partially suspended in the pipe. When the particle diameter was 12 mm, the mass of the particle was relatively large. Its own inertial force was also relatively large and the air was weaker in carrying the particle. When the particles of 12 mm in diameter passed through the bend, the particles almost all moved along the outside of the pipe wall due to inertia. After the particles left the bend, the particles with a size of 7 mm were quickly blown up by the air and suspended in the pipe because of their small mass. On the other hand, particles with a size of 12 mm showed a longer distance before being suspended in the pipeline again. According to the analysis, due to the particle masses of the two different particle sizes being different, the large particles had a large mass and inertia and almost all of them moved along the outside of the pipe wall when passing through the bend. Conversely, due to the small mass and inertia of the small particles, a small number of particles would not move close to the outside of the pipe wall under the carrying effect of air when passing through the elbow. This phenomenon gives an explanation for why large particles cause more serious wear than small particles.

#### 4.2. Pressure Distribution

According to the simulation results, the pressure cloud diagram of the pipeline in Figure 4 was obtained. The pressure was highest at the entrance of the pipe and then gradually decreased along the direction of airflow. Because the upper side of the pipe

curvature was near the entrance, the inlet had stronger air pressure. On the other hand, the lower side of the pipe curvature was near the outlet, so its pressure was low. Moreover, as the particle flowed through the pipe, friction occurred with the pipe wall and a potential energy loss of airflow was produced. Therefore, the pressure reduced along the direction of airflow from the upper side to the lower side of the bend. In addition, when the particles passed through the bend, the particles hit the left side of the tube wall and formed contact pressure with the pipe wall because of inertia. The left pressure on the outside of the pipe wall was greater than the right side.



**Figure 4.** Pipeline pressure distribution.

Figure 5 indicates the relationship between the pressure at the pipe inlet and the wind speed. The curve of inlet pressure with wind speed showed an increasing trend. The inlet pressure increased with an increase in wind speed; thus, the higher the wind speed, the higher the wind pressure. According to the analysis, the pressure on the same part of the pipe was different when the wind speed was different. Pressure increased with increasing wind speed. As the wind velocity became larger, the velocity of the solid particles became larger. Thus, the kinetic energy of the solid became larger when the solid particles hit the wall of the pipe.

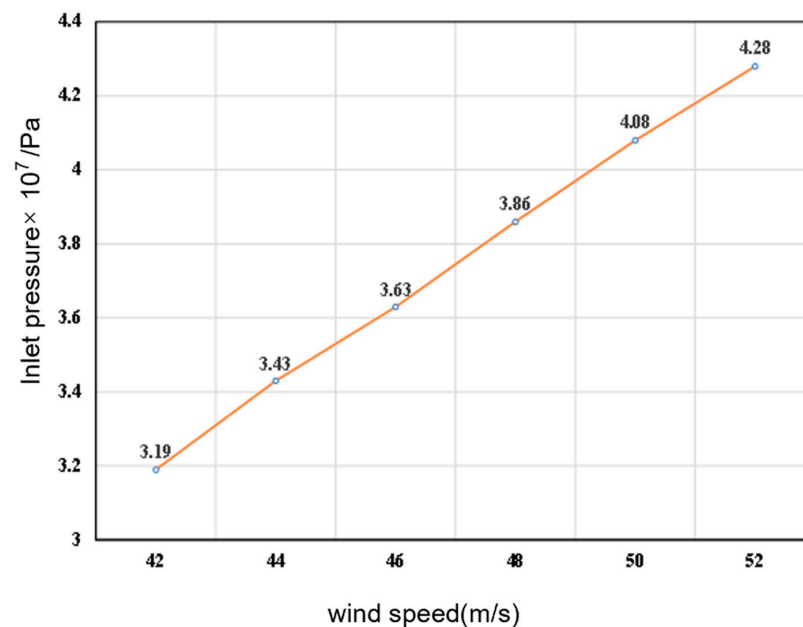
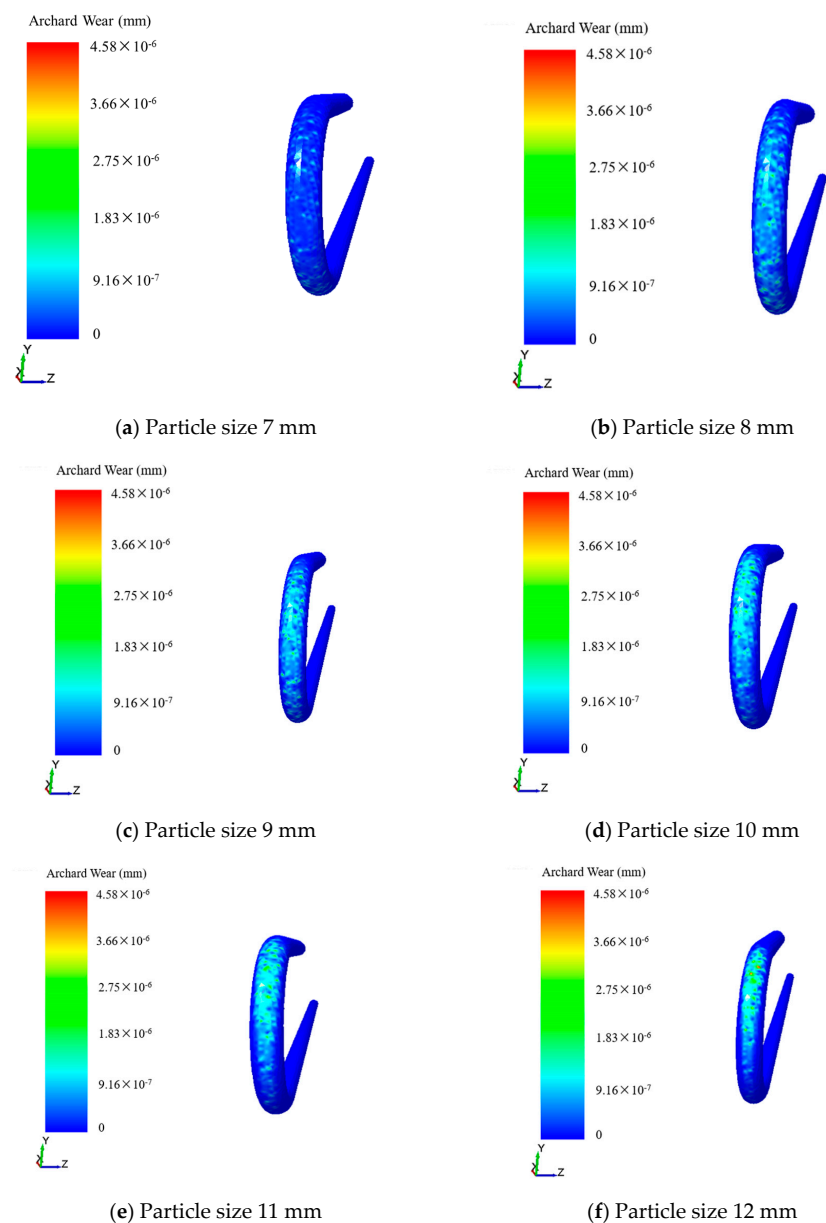


**Figure 5.** Inlet pressure as a function of wind speed.

#### 4.3. Effects of Particle Diameter on Pipe Wear

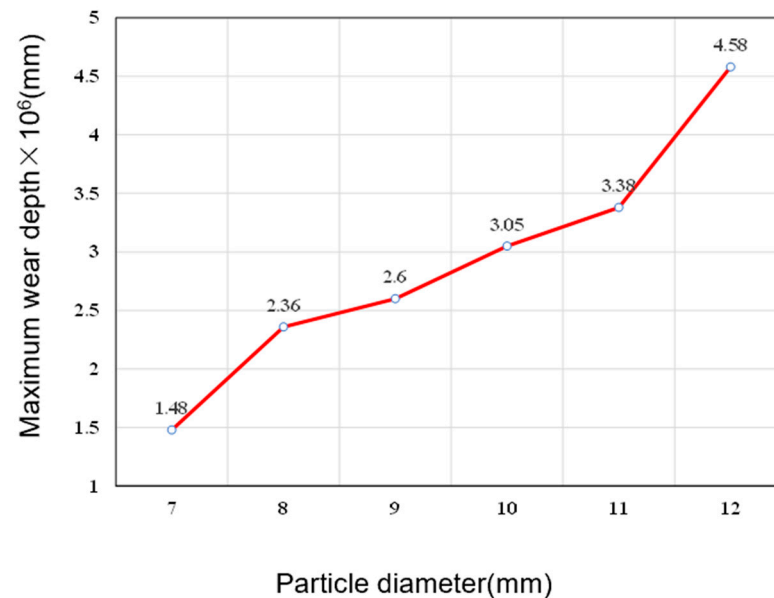
To conduct the simulations to analyze the effects of different particle diameters on pipe wear, particles with diameters of 7, 8, 9, 10, 11 and 12 mm were selected. According to the simulation results, wear clouds with different particle diameters were obtained as shown in Figure 6. The pipe wear over almost the entire outer part of the bend can be seen in

Figure 6a, but the amount of wear was low in the particles with diameters of 7 mm. When the particle diameter was 8 mm, Figure 6b demonstrates that the wear position of the pipe still occupied the entire outer part of the bend, but the amount of wear was significantly larger than that from the 7 mm diameter particles. For the particles with diameters of 9 mm, the wear of the pipe continued to increase as indicated in Figure 6c. Until the particle diameter increased to 10 mm, the wear of the pipe still continued to increase, with Figure 6d indicating that the wear location of the pipe was almost entirely concentrated in the upper part of the bend. When the particle diameters increased to 12 mm, Figure 6f clearly reveals that the location of wear in the pipe was more concentrated and the amount of wear was greater than that of the 11 mm diameter particles in Figure 6e. The whole phenomenon in Figure 6 implies that due to the different inertia of particles with different diameters (larger particles having a large inertia), the particles with larger diameters contacted more with the pipe wall than small particles when passing through the elbow, resulting in larger pressure and larger wear.



**Figure 6.** Wear clouds of particles with different diameters.

According to the maximum wear depth of the pipeline under different particle sizes, the relationship between the maximum wear depth of the pipeline and the particle diameter was obtained as shown in Figure 7.



**Figure 7.** Maximum wear depth of the pipe as a function of particle diameter.

The maximum wear depth of the pipe became larger as the particle diameter increased. According to analysis, solid particles were mainly subject to their own inertial forces and fluid traction in pipeline transport. When the particles were passing through the bend, the traction of the fluid caused the particles to move in the direction of the airflow. Its own inertial force pushed the particles to strike the inner wall of the elbow. When the particle was small, the mass of the particle was also low, the airflow had a high carrying capacity for particles, this particle was subjected to traction, the inertial force of the particle itself was relatively small and the particles separated from the fluid relatively late. So the velocity of the particles hitting the bend wall was small, the impact angle when hitting the wall was small, and the impact position in bend was also more backward. Thus, when the particle diameter was small, the pipe wear was also slight, and the wear position was near the lower part of the bend. When the particle diameter increased, the mass of the particle increased, the inertial force of the particle increased, the carrying capacity of airflow to the particles decreased, the impact velocity of solid particles on wall surface increased, the amount of pipe wear also increased, the particles were separated from the fluid earlier and the particles hit the wall near the top of the bend.

Figure 8 illustrates that the maximum wear position of the bend part is between  $90^\circ$  and  $135^\circ$  for the particle of 7 mm diameter. The position of maximum wear was shifted upwards to between  $45^\circ$  and  $135^\circ$  for the particles of 8 mm diameter. The most severe wear position was shifted up to between  $0^\circ$  and  $90^\circ$ , when the particle size increased to 9 mm. For the particles of 10 mm and 11 mm, the most severe wear position was still between  $0^\circ$  and  $90^\circ$ , but it was significantly higher than that of the particle of 9 mm size. When the particle size increased to 12 mm, the position of maximum wear was completely shifted up to  $0^\circ$ – $45^\circ$ , closing to  $30^\circ$ .

As the particle diameter increased, the main position of wear gradually shifted upward. As the particle size increased, the mass of the particles also increased, the inertial force of the particle increased and the carrying effect of airflow on them weakened. After entering the elbow, the separation of particles and wind was earlier. The comparison in Figure 9 between the particle size of 7 mm and 12 mm shows that the particle of 12 mm size is separated from the fluid earlier than that of the particle of 7 mm size. Therefore, as the particle size increased, the position of the particle hitting the elbow moved up in bend.

In summary, the degree of pipe wear increased with the increase in shotcrete coarse aggregate diameter. At the same time, the change in particle diameter was critical to the change in wear location. When the particle size was 7 mm, the slight wear position almost covered the whole bend. The particle size increased and the wear position gradually moved up. When the particle size increased to 12 mm, the wear was almost all concentrated on the outer part of the upper half of the bend. When the particle size was 7 mm, the most severe wear position was located near  $135^\circ$ . The position of the most serious wear gradually moved up with the particle size gradually increased. When the particle size increased to 12 mm, the position of the most serious wear moved up to about  $30^\circ$ .

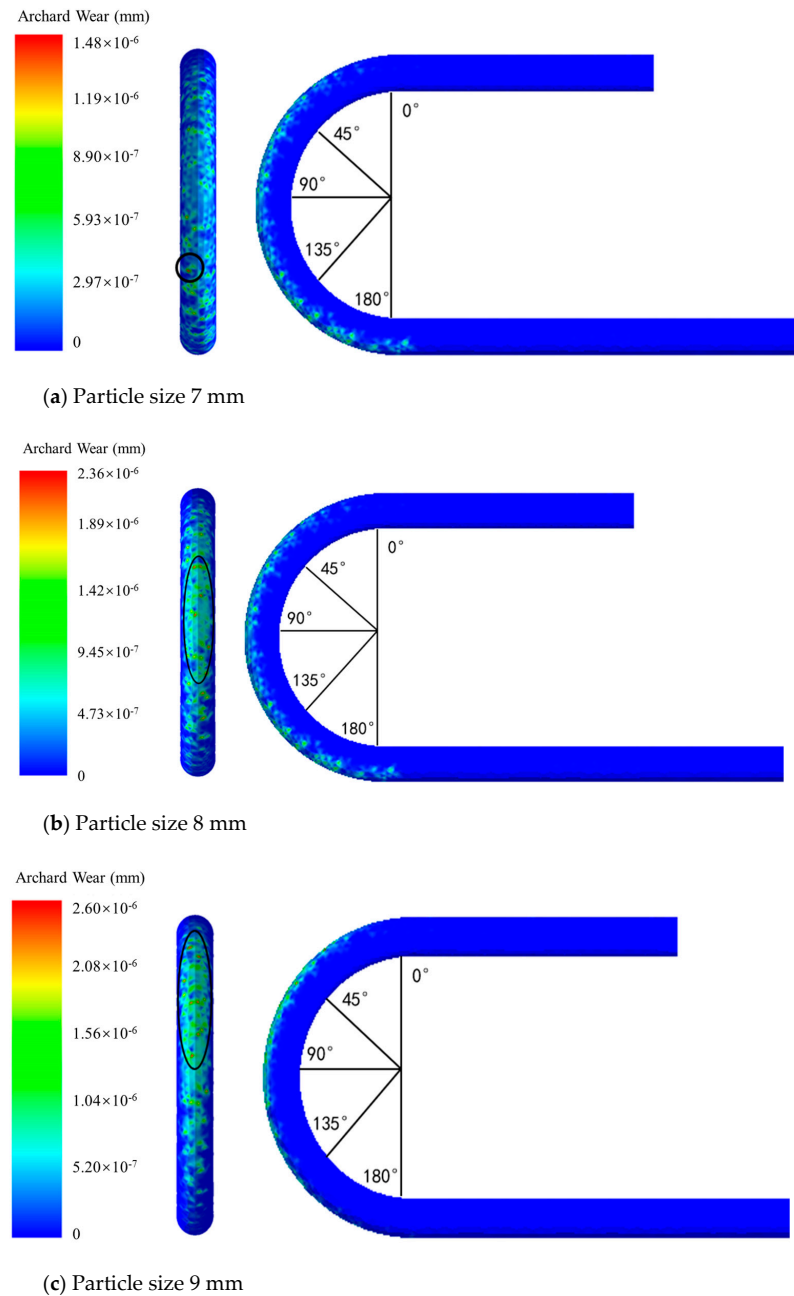
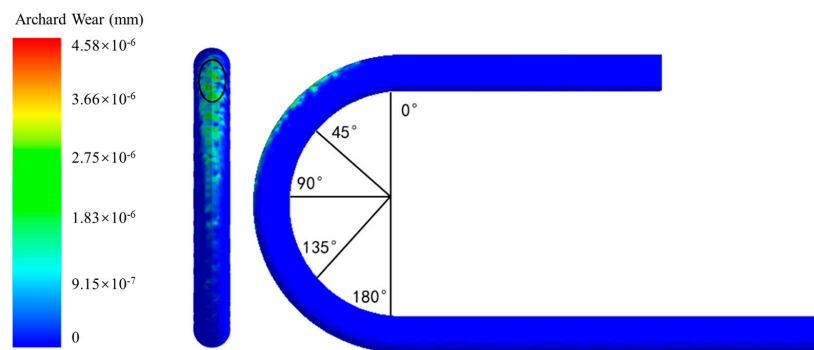
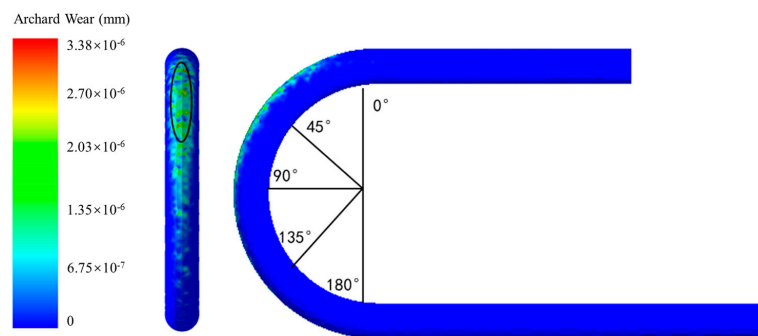
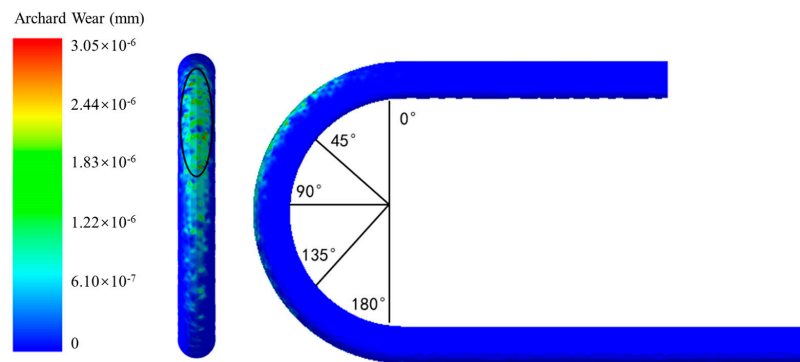
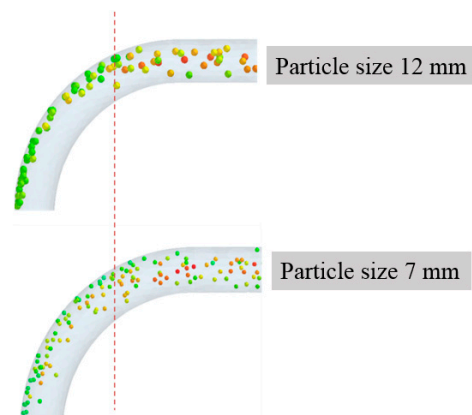


Figure 8. Cont.



**Figure 8.** Wear location distribution of particles with different diameter.



**Figure 9.** Particle distribution comparison between 12 mm (**up**) and 7 mm (**down**) size.

#### 4.4. Effect of Wind Speed on Pipe Wear

To analyze the effect of wind speed on the wear of conveying pipes, a radius of curvature of 250 mm was specified for the bend and the diameter of the particles was 12 mm. The wind speeds of 42 m/s, 44 m/s, 46 m/s, 48 m/s, 50 m/s and 52 m/s were selected by the control variable method for simulation. According to the simulation results, the influence law of different wind speed on pipe wear is shown in Figure 10.

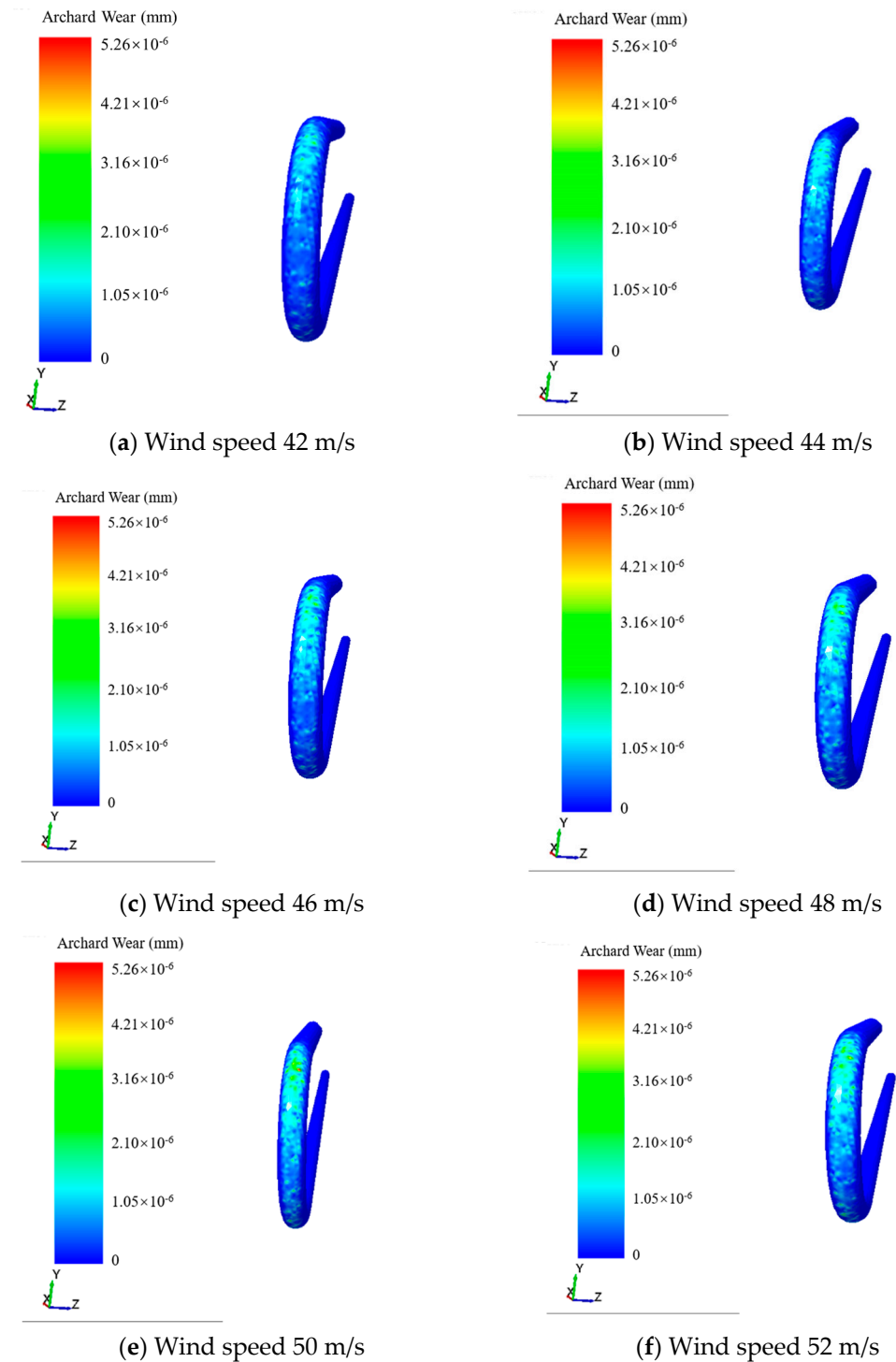


Figure 10. Wear and tear at different wind speeds.

The variation in wind speed has almost no effect on the location of the pipe wear for a constant particle diameter as shown in Figure 10. The entire outside of the bend was worn. The main wear location was still concentrated in the upper part of the bend. The degree of wear increased with the increase in wind speed. According to the maximum wear depth under different wind speeds, the change in the maximum wear depth of the pipeline with the wind speed is shown in Figure 11.

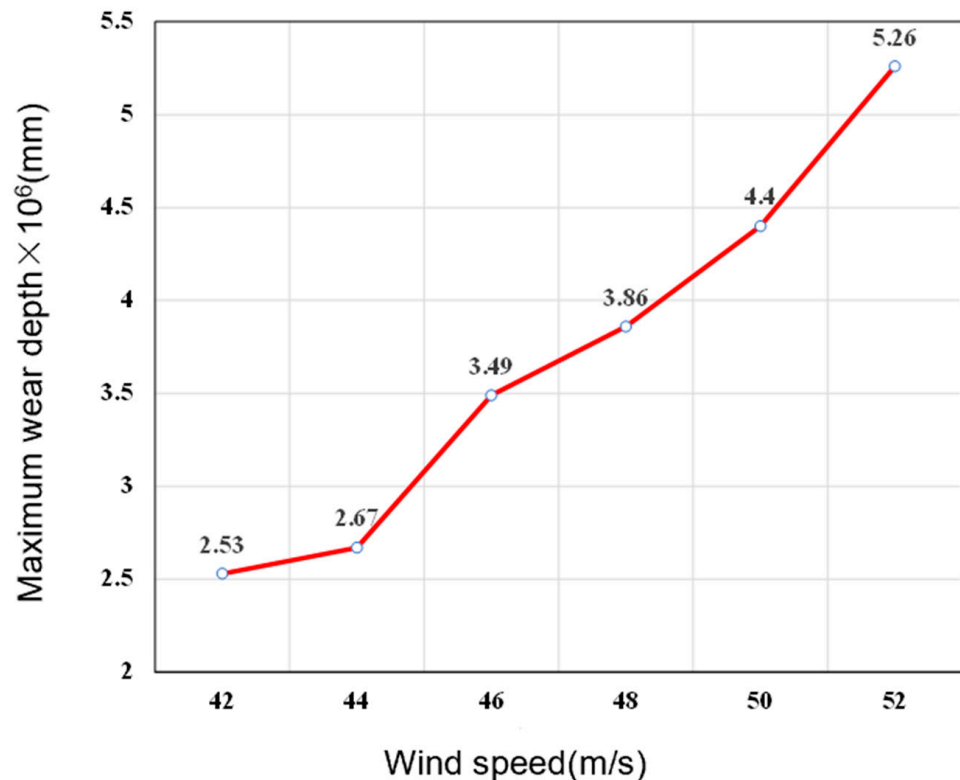
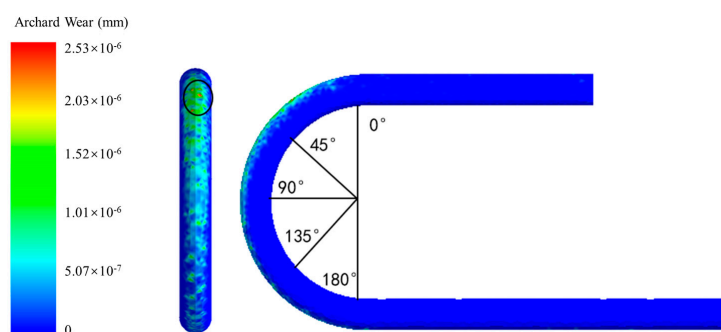


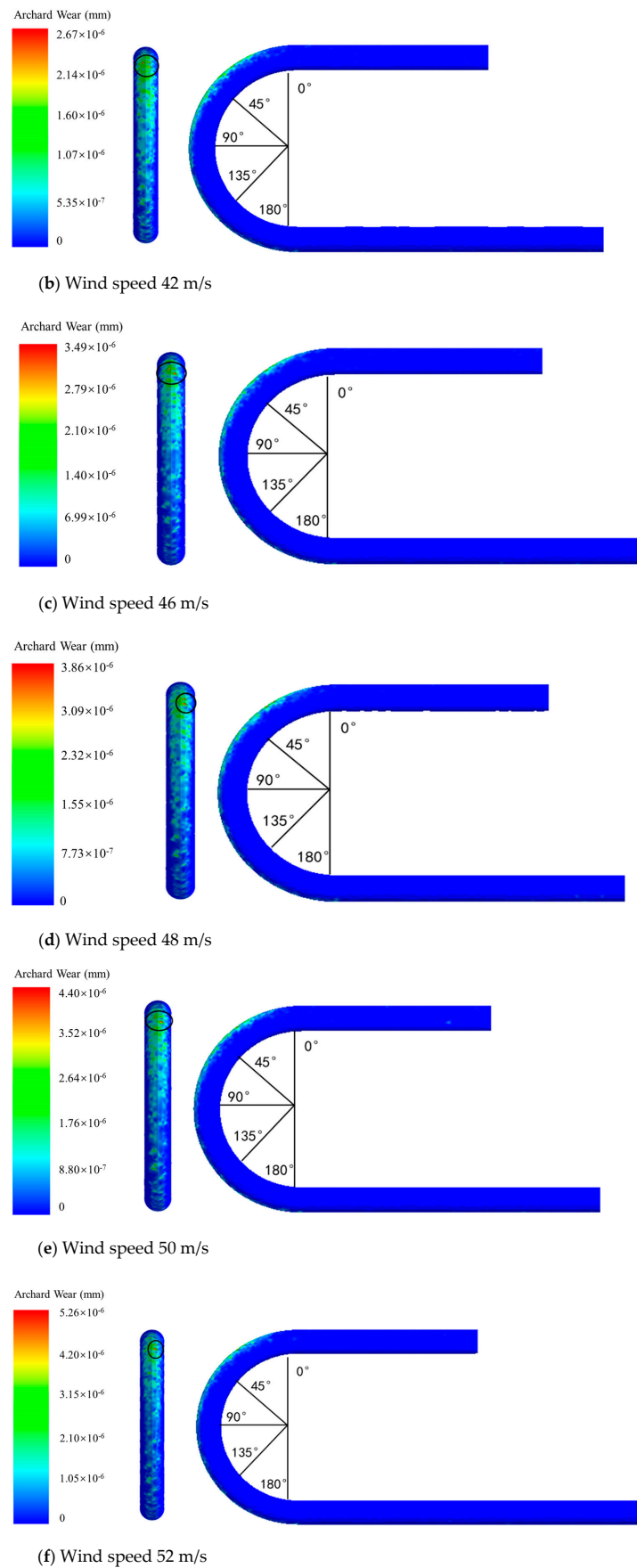
Figure 11. Maximum wear depth of the pipe with different wind speed.

Figure 11 shows that the maximum wear depth of the pipe increased gradually with the increase in airflow speed. Wear was caused by the collision and friction between solid particles and the pipe wall. All other conditions being equal, the velocity of the solid particles increased as the wind velocity increased. At the same time, since the energy of the solid particles hitting the elbow at a high speed was larger, it was easier to cause more serious wear. It can be seen that the change in wind speed had little effect on the wear position by analyzing Figure 12. The main wear position was still located at 0–90° and the position with the greatest wear depth was located at 0–45°.



(a) Wind speed 42 m/s

Figure 12. Cont.



**Figure 12.** Wear positions at different wind speeds.

In summary, as the wind speed increased, the maximum wear depth of the pipe increased. The degree of wear was aggravated and the change in wind speed had almost no effect on the location of the wear in the bend.

#### 4.5. Influence of Elbow Curvature Radius on Pipe Wear

When analyzing the influence of the elbow curvature radius on the wear of the inner wall of the bend pipe, the size of the wind speed was specified as 50 m/s, the particle diameter was 12 mm, and then, the elbow curvature radii were chosen as 200 mm, 250 mm and 300 mm. By conducting simulations, different simulation results were obtained. From the analysis, wear clouds under the conditions of the same particle diameter and wind speed are shown in Figure 13.

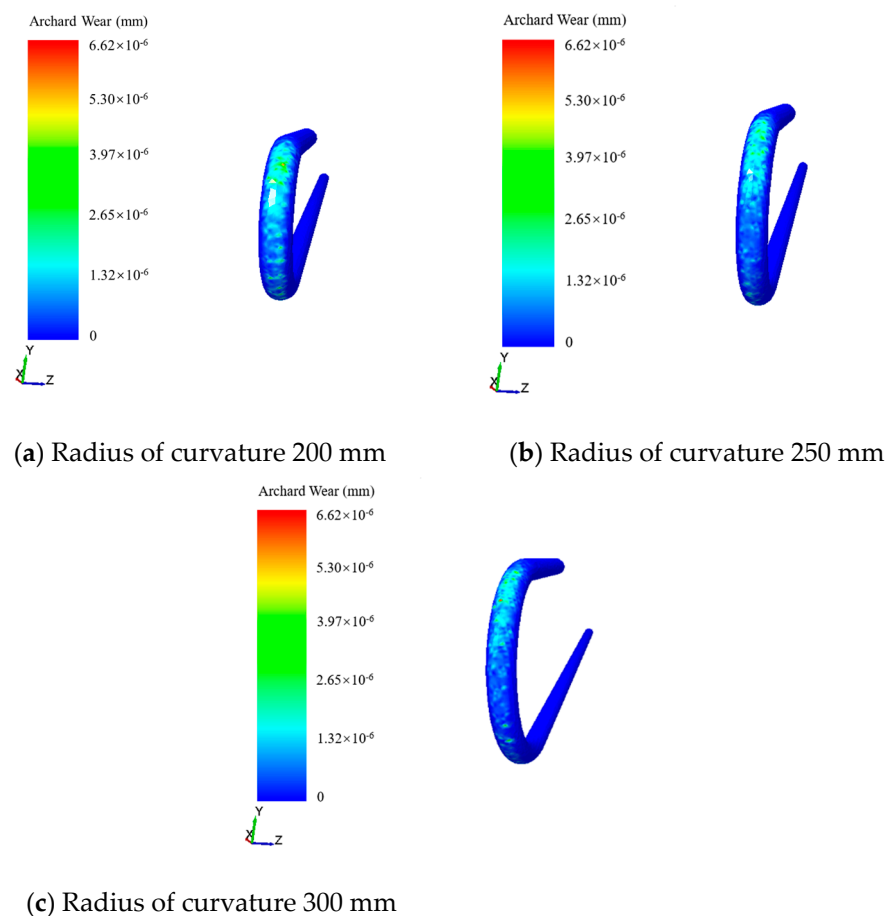


**Figure 13.** Wear clouds under different curvature radii.

The wear area was mostly concentrated in the upper part of the bend when the curvature radius was 200 mm and the wear amount of the bend as a whole was larger. When the curvature radius increased to 250 mm, the location of the wear area did not change much and remained concentrated in the upper part of the bend, but the overall wear was reduced compared to that of the 200 mm curvature radius. When the curvature radius increased to 300 mm, the overall wear decreased compared to the 250 mm curvature radius, but the difference in bend wear was not significant.

When the elbow curvature radius was 200 mm, the maximum wear depth of the pipeline was  $5.83 \times 10^{-6}$  mm. When the elbow curvature radius was 250 mm, the maximum wear depth of the pipeline was  $4.47 \times 10^{-6}$  mm. When the elbow curvature radius was 300 mm, the maximum wear depth of the pipeline was  $6.58 \times 10^{-6}$  mm. The relationship between the maximum wear depth and the elbow curvature radius is shown in Figure 14.

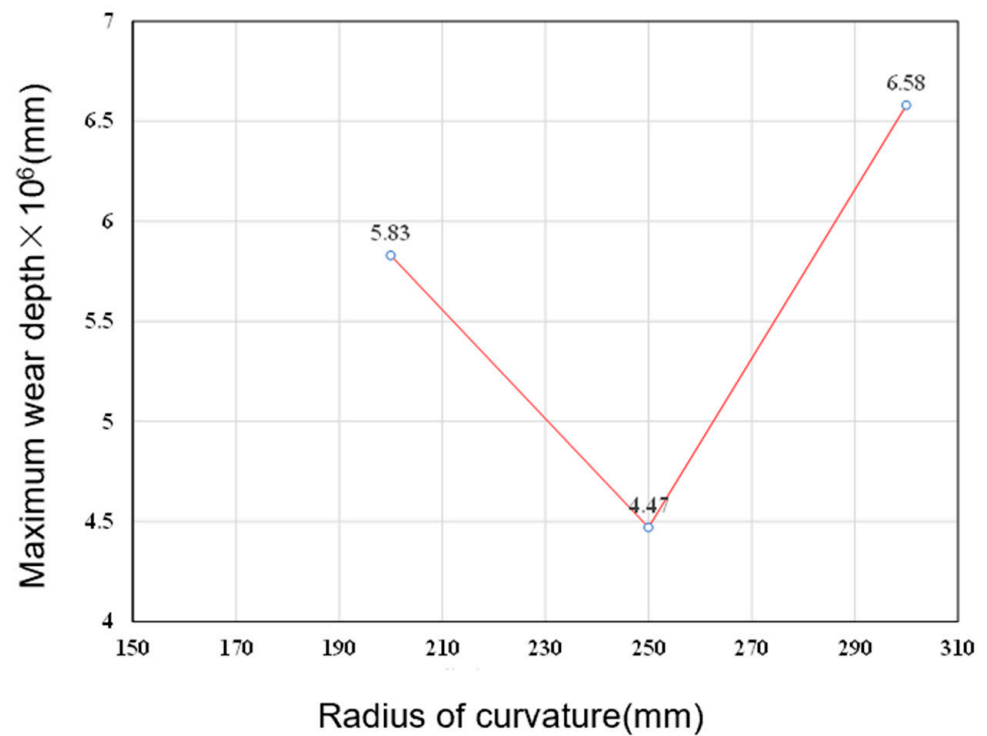
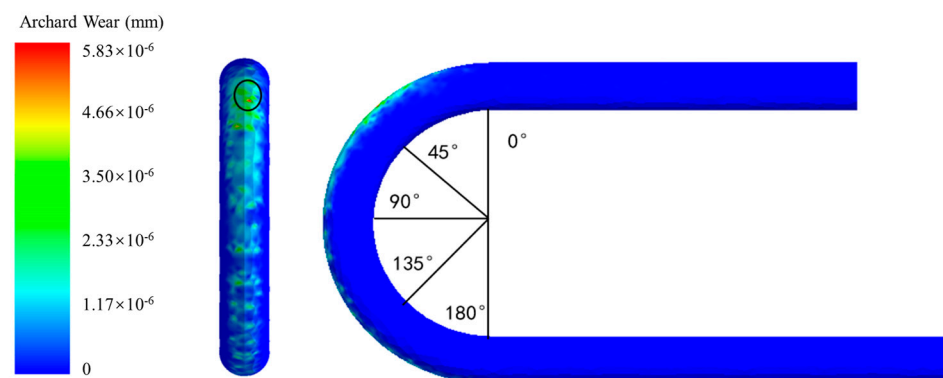


**Figure 14.** Relationship between maximum wear depth and elbow curvature radius.

Figure 14 shows that the maximum wear depth was minimal at an elbow curvature radius of 250 mm when compared to the wear at elbow curvature radii of 200 mm and 300 mm. The maximum wear depth did not show a clear trend with respect to the elbow curvature radius. The maximum wear depth of the pipe decreased when the elbow curvature radius was increased from 200 mm to 250 mm. When the elbow curvature radius increased, the bend was smoother, the impact angle of the particles on the pipe wall was smaller and the degree of wear was also smaller. However, the maximum wear depth increased when the elbow curvature radius increased to 300 mm, so it is not true that the degree of wear became less as the elbow curvature radius became larger.

It can be seen from Figure 15 that changes in the curvature radius have less of an influence on the position of pipe wear. At all three radii of the curvature in this study, the major wear locations were between  $0^\circ$  and  $90^\circ$  and the most severe wear location was between  $0^\circ$  and  $45^\circ$ , at approximately  $30^\circ$ .



(a) Radius of curvature 200 mm

**Figure 15.** Cont.

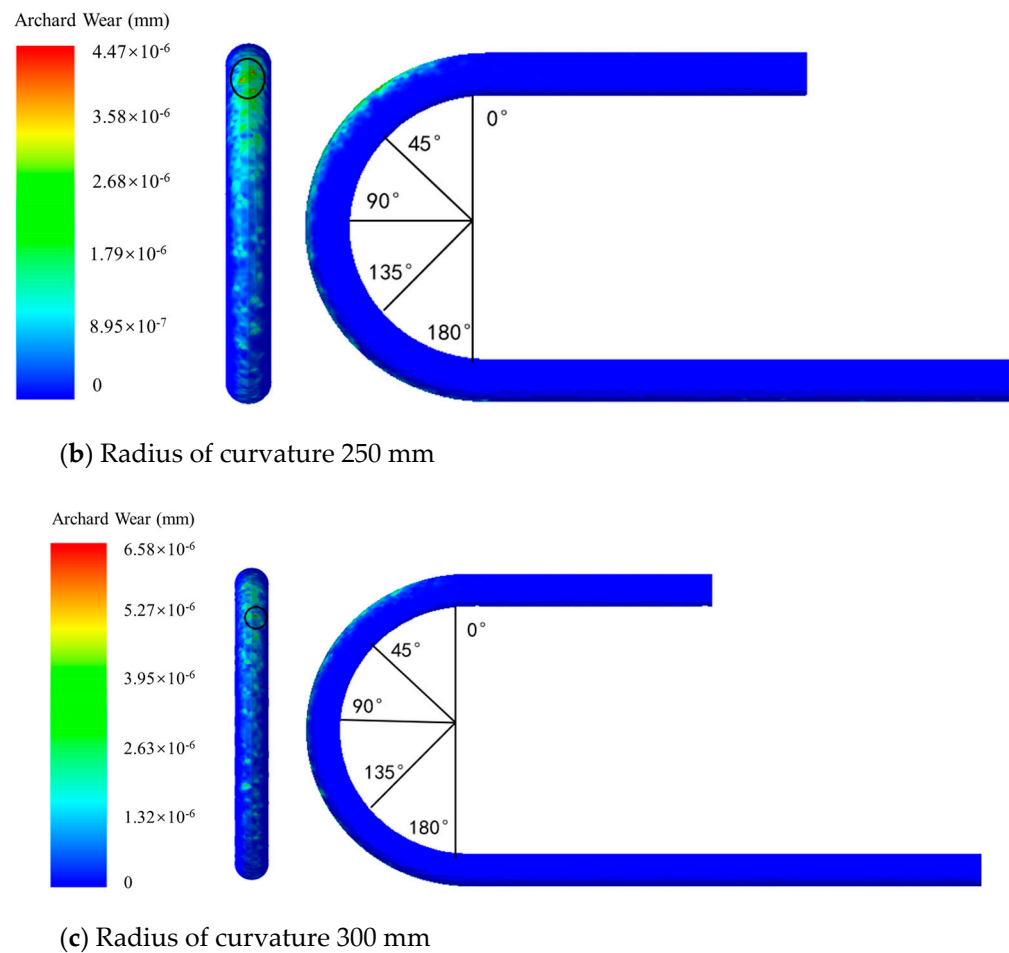


**Figure 15.** Wear positions under different radii of the curvature.

According to the results of this simulation, the overall wear degree and the maximum wear depth of the elbow decreased when the elbow curvature radius increased appropriately. Moreover, if the elbow curvature radius was too large, the maximum depth of wear would also increase. So, increasing the elbow curvature radius did not ensure a better effect. The elbow curvature radius had almost no effect on the position of wear. The main wear position was on the outside of the upper part of the bend and the most serious wear position was around  $30^\circ$ .

## 5. Pipe Wear Control Strategy

In the process of conveying shotcrete, the bend pipe is the most easily worn position. It is very easy for solid particles to collide with the pipe wall at the bend and cause wear. If the inner wall of the pipeline is seriously worn, the wear is easy to wear through, affecting material transportation and resulting in safety accidents. Effective measures must be taken to reduce the wear of pipes. Control measures were proposed to reduce the wear of shotcrete-conveying pipes based on some wear laws derived from the previous section and the wear of pipes in actual projects.

### (1) Control the size of aggregates

The wear of shotcrete-conveying pipes is mainly caused by the collision and friction between the coarse aggregate and pipe wall, with a greater size of the aggregate having a greater impact on the wear of the pipe. As obtained from the study on the effect of particle diameter on the wear condition of the pipe in the previous section, the maximum wear depth of the pipe increased from  $1.48 \times 10^{-6}$  mm to  $4.58 \times 10^{-6}$  mm when the diameter of particles increased from 7 mm to 12 mm, and the degree of wear became larger. In the particle size range studied in this simulation, the maximum wear depth of the pipes

increased with an increase in particle diameter. In the case of meeting the requirements of shotcrete for coarse aggregate grading, minimizing the amount of coarse aggregate could effectively reduce the degree of pipe wear.

(2) Control the size of the wind speed

In the study of wind speed affecting pipe wear, it was known that the maximum wear depth of the pipe increased from  $2.53 \times 10^{-6}$  mm to  $5.26 \times 10^{-6}$  mm when the wind speed increased from 42 m/s to 52 m/s. In the wind speed range of this simulation study, the maximum wear depth of the pipe wall increased with increasing wind speed. As the velocity of solid particles increased, more energy was applied to hit the pipe wall. An appropriate reduction in wind speed could effectively reduce the degree of pipe wear and the reduction in wind speed could also reduce the energy consumption of shotcrete. However, when the wind speed was too small, the shotcrete would accumulate at the bottom of the pipe under the action of gravity. Therefore, the wind speed should not be reduced indefinitely to ensure normal material flow and also to meet the technical requirements of shotcrete.

(3) Control the bend radius

When using a bend, the bend with a larger radius of curvature could be chosen. When the curvature radius of the pipeline was 200 mm, the maximum wear depth of the pipeline was  $5.83 \times 10^{-6}$  mm. When the curvature radius of the pipeline was 250 mm, the maximum wear depth of the pipeline was  $4.47 \times 10^{-6}$  mm. When the curvature radius of the pipeline was 300 mm, the maximum wear depth of the pipeline was  $6.58 \times 10^{-6}$  mm. The proper radius of curvature should be selected according to the actual working conditions.

(4) Other control measures

In the process of material transportation, improvements are made in terms of the shape of the aggregate, the wear resistance of the pipe itself and the construction of the pipe foundation. When the aggregate shape is irregular, it is likely to cause cutting wear on the pipe wall. In order to reduce the degree of wear of the pipe, smooth surface pebbles could be chosen as coarse aggregate under the condition of meeting the technical requirements of shotcrete. Selecting piping materials with good wear resistance could effectively reduce the degree of piping wear. A layer of wear-resistant material could be wrapped around the outside of the pipe to form a double-layer casing inside and outside to improve the wear resistance of the pipe. For localized wear and leaks that occur in the pipeline, wear repair agents are needed. Scoring thread lines on the inner wall of the tube could change the slurry flow state, thus reducing the deposition of solids and reducing the impact energy of the material on the tube wall.

## 6. Conclusions

In pneumatic shotcrete pipe conveying, pipe wear is an inevitable problem. In this paper, three influencing factors (the particle diameter, wind speed and radius of the curvature of the bend) were studied in depth and a systematic study of the wear regularity of conveying pipelines of shotcrete was carried out. The main findings are as follows:

- (1) In order to analyze the effect of particle size on pipe wear, six different particle diameters (7, 8, 9, 10, 11 and 12 mm) were selected to simulate pipe wear. According to the simulation results, the degree of pipe wear increased with the increase in particle diameter. Changes in particle diameter affected the location of pipe wear. As the particle size increased, the location of wear gradually concentrated from the outside of the entire bend to the outside of the upper part of the bend at the beginning. The maximum depth of wear was around  $135^\circ$  at a particle size of 7 mm. As the particle size increased, the position of the maximum wear depth gradually moved up until the most severe wear position moved near  $30^\circ$  when the particle diameter was 12 mm.
- (2) For the simulation of wind speed, six different sets of wind speeds were selected: 42, 44, 46, 48, 50 and 52 m/s. In the wind speed range of this simulation study, the wear of the pipe increased with the increase in wind speed. When the particle diameter was the same, the change in wind speed had little effect on the wear position of the

pipe. The centralized wear position was located in the upper part of the bend and the most serious wear position was in the range of 0–45° of this bend.

- (3) Three different sets of radii of the curvature (200 mm, 250 mm, 300 mm) were used to simulate the effect of the bend radius of the curvature on pipe wear. According to the simulation results, the maximum wear depth and the overall wear of the pipe decreased when the radius of the curvature increased from 200 mm to 250 mm. When the radius of the curvature increased to 300 mm, the maximum wear depth increased and the change in the radius of the curvature had almost no effect on the wear position.
- (4) Based on the simulation results and the actual wear of the pipeline in the actual project, the control measures for pipeline wear are proposed as a way to reduce the degree of pipeline wear and extend the life of pipelines, including particle size control, convey speed control, bend radius control and other measurements.

**Author Contributions:** Writing—original draft, Y.H. and G.L.; Software, Y.H.; Data curation, S.S. and X.C.; Formal analysis, S.S.; Methodology, J.S.; Investigation, J.S. and Q.X.; Funding acquisition, G.L. and J.L.; Supervision, G.L.; Writing—review & editing, J.L. All authors have read and agreed to the published version of the manuscript.

**Funding:** This research was funded by National Natural Science Foundation of China (Grant No. 52104206); 2022 open project of the Key Laboratory of Dust Hazard Engineering Protection of the National Health Commission (KLECDH2022020102); Special funds from the Taishan Scholar Project; Qingdao West Coast New Area Source Innovation Project (2020-89, 2021-111); and Youth Innovation Team Program of Shandong Provincial Colleges and Universities.

**Institutional Review Board Statement:** Not applicable.

**Informed Consent Statement:** Not applicable.

**Data Availability Statement:** Not applicable.

**Acknowledgments:** The author would like to thank the teachers and students in the collegae of safety and environmental engineering of Shandong University of Science and Technology for their active participation and help in this study.

**Conflicts of Interest:** The authors declare no conflict of interest.

## References

1. Kuang, S.; Zhou, M.; Yu, A. CFD-DEM modelling and simulation of pneumatic conveying: A review. *Powder Technol.* **2020**, *365*, 186–207. [[CrossRef](#)]
2. Song, C.X.; Liu, D.Y.; Ma, J.L.; Chen, X.P. CFD-DEM simulation of flow pattern and particle velocity in a fluidized bed with wet particles. *Powder Technol.* **2017**, *314*, 346–354. [[CrossRef](#)]
3. Weimin, C.; Guoming, L.; Lianju, C. Research progress of mine shotcrete dust control technology. *Saf. Coal Mines* **2020**, *10*, 87–97.
4. Sun, Z.; Chen, L.; Yu, X.; Liu, G.; Ma, H. Study on optimization of shotcrete loading technology and the diffusion law of intermittent dust generation. *J. Clean. Prod.* **2021**, *312*, 127765. [[CrossRef](#)]
5. Yonghong, Y.; Peng, D.; Hetao, H.; Zhangyong, M.; Yan, L. Experimental study on shear resistance of bolt connector in steel-concrete composite beam. *J. Shandong Univ. Sci. Technol.* **2021**, *2*, 51–59.
6. Santo, N.; Kalman, H. Blinded T-bends flow patterns in pneumatic conveying systems. *Powder Technol.* **2017**, *321*, 347–354. [[CrossRef](#)]
7. Salman, A.D.; Hounslow, M.J.; Verba, A. Particle fragmentation in dilute phase pneumatic conveying. *Powder Technol.* **2002**, *126*, 109–115. [[CrossRef](#)]
8. Kotzur, B.A.; Berry, R.J.; Zigan, S.; García-Triñanes, P.; Bradley, M.S.A. Particle attrition mechanisms, their characterisation, and application to horizontal lean phase pneumatic conveying systems: A review. *Powder Technol.* **2018**, *334*, 76–105. [[CrossRef](#)]
9. Messa, G.V.; Yang, Q.; Adedeji, O.E.; Chára, Z.; Duarte, C.A.R.; Matoušek, V.; Rasteiro, M.G.; Sanders, R.S.; Silva, R.C.; de Souza, F.J. Computational Fluid Dynamics Modelling of Liquid-Solid Slurry Flows in Pipelines: State-of-the-Art and Future Perspectives. *Processes* **2021**, *9*, 1566. [[CrossRef](#)]
10. Shi, Q.; Sakai, M. Recent progress on the discrete element method simulations for powder transport systems: A review. *Adv. Powder Technol.* **2022**, *33*, 103664. [[CrossRef](#)]
11. Yue, Y.H.; Zhang, C.X.; Shen, Y.S. CFD-DEM model study of gas-solid flow in a spout fluidized bed with an umbrella-like baffle. *Chem. Eng. Sci.* **2020**, *230*, 116234. [[CrossRef](#)]

12. Tang, Q.; Twumasi, J.O.; Wang, X.; Yu, T.; Hu, J. Finite element simulation of photoacoustic fiber optic sensors for surface corrosion detection on a steel rod. In Proceedings of the Nondestructive Characterization & Monitoring of Advanced Materials, Aerospace, Civil Infrastructure, & Transportation, Denver, CO, United States, 5–8 March 2018; Volume XII. [\[CrossRef\]](#)
13. Vega, F.G.; Carlevaro, C.M.; Sánchez, M.; Pugnali, L.A. Stability and conductivity of proppant packs during flowback in unconventional reservoirs: A CFD–DEM simulation study. *J. Pet. Sci. Eng.* **2021**, *201*, 108381. [\[CrossRef\]](#)
14. Grötzbach, M. Solid particle erosion and erosion-corrosion of materials. *ASM Int.* **1995**, *47*, 715.
15. Tilly, G.P. A two stage mechanism of ductile erosion. *Wear* **1973**, *23*, 87–96. [\[CrossRef\]](#)
16. Zhang, L.; Sun, Y.Q.; Ming, L.; Liu, M.; Wang, L.Q. Research on the influence of cutting parameters on chips in the process of diamond bead cutting pipeline steel. *Diam. Relat. Mater.* **2021**, *111*, 108220.
17. Hutchings, I.M. A model for the erosion of metals by spherical particles at normal incidence. *Wear* **1981**, *70*, 269–281. [\[CrossRef\]](#)
18. McLaury, B.S. *Predicting Solid Particle Erosion Resulting from Turbulent Fluctuations in Oil Filed Geometries*; The University of Tulsa: Tulsa, Oklahoma, 1996.
19. Chen, X.; McLaury, B.S.; Shirazi, S.A. Application and experimental validation of a computational fluid dynamics (CFD)-based erosion prediction model in elbows and plugged tees. *Comput. Fluids* **2004**, *33*, 1251–1272. [\[CrossRef\]](#)
20. Kuang, D. Erosion wear analysis of solid particles in liquid-solid two-phase flow of right-angle bend pipe. *Oil Gas Storage Transp.* **2013**, *32*, 241–246.
21. Liu, X.F.; Zhou, J.F.; Gao, S.Q.; Zhao, H.L.; Liao, Z.Y.; Jin, H.Z.; Wang, C. Study on the Impact Wear Characteristics of Catalyst Particles at 90 degrees Elbow via, C.F.D-DEM Coupling Method. *J. Appl. Fluid Mech.* **2022**, *15*, 221–230.
22. Tan, Y.Q.; Zhang, H.; Yang, D.M.; Jiang, S.Q.; Song, J.H.; Sheng, Y. Numerical simulation of concrete pumping process and investigation of wear mechanism of the piping wall. *Tribol. Int.* **2012**, *46*, 137–144. [\[CrossRef\]](#)
23. Wang, Y.Y.; Wang, Y.; Yang, G.F.; Ruan, Z.E.; Wang, Z.Q. Effect of cement-to-tailings ratio and flow rate on the wear performance of filling pipeline. *Powder Technol.* **2022**, *397*, 117027. [\[CrossRef\]](#)
24. Chen, L.J.; Sun, Z.J.; Ma, H.; Pan, G.; Li, P.C.; Gao, K. Flow characteristics of pneumatic conveying of stiff shotcrete based on, C.F.D-DEM method. *Powder Technol.* **2022**, *397*, 117109. [\[CrossRef\]](#)
25. Singh, J.; Kumar, S.; Singh, J.P.; Kumar, P.; Mohapatra, S.K. CFD modeling of erosion wear in pipe bend for the flow of bottom ash suspension. *Part. Sci. Technol.* **2019**, *37*, 275–285. [\[CrossRef\]](#)
26. Wang, Z.C.; Chen, Y.; Sun, J.; Xia, H.C. Analysis of erosion wear of filling slurry on reducing pipes. *J. Shandong Univ. Sci. Technol.* **2022**, *41*, 39–46.
27. Naveh, R.; Tripathi, N.M.; Kalman, H. Experimental pressure drop analysis for horizontal dilute phase particle-fluid flows. *Powder Technol.* **2017**, *321*, 355–368. [\[CrossRef\]](#)
28. Li, M.Z.; He, Y.P.; Liu, Y.D.; Huang, C. Analysis of transport properties with varying parameters of slurry in horizontal pipeline using, A.N.SYS fluent. *Part. Sci. Technol.* **2020**, *38*, 726–739. [\[CrossRef\]](#)
29. Zhou, H.J.; Xiong, Y.Q. Conveying mechanisms of dense-phase pneumatic conveying of pulverized lignite in horizontal pipe under high pressure. *Powder Technol.* **2020**, *363*, 7–22. [\[CrossRef\]](#)
30. Sun, H.Y.; Ma, H.Q.; Zhao, Y.Z. DEM investigation on conveying of non-spherical particles in a screw conveyor. *Particuology* **2022**, *65*, 17–31. [\[CrossRef\]](#)
31. Chunjie, W. FLUENT-based study of pipe wear in refrigeration systems. *China Plant Eng.* **2018**, *23*, 132–134.
32. Ma, G.G.; Ma, H.; Sun, Z.J. Simulation of Two-Phase Flow of Shotcrete in a Bent Pipe Based on a, C.F.D-DEM Coupling Model. *Appl. Sci.* **2022**, *12*, 3530. [\[CrossRef\]](#)
33. Liu, Z.Y.; Yin, P.M.; Wei, X.B.; Ding, Q.; Cao, X.Q.; Zhang, G.A.; Xue, Q. Simultaneous deposition of, D.L.C film on the internal surface of multiple pipes. *Diam. Relat. Mater.* **2022**, *127*, 109187. [\[CrossRef\]](#)
34. Guo, Z.; Zhang, J.; Li, H.; He, H. A comprehensive evaluation of the anti-erosion characteristics of several new structural elbows in the pneumatic conveying system. *Powder Technol.* **2022**, *412*, 117976. [\[CrossRef\]](#)
35. Zhou, F.; Li, J.; Yang, D.; Li, Y.; Luo, J. Experimental study on collision characteristics of large coal particles (7–15 mm) in 90° elbows of pneumatic conveying systems. *Powder Technol.* **2022**, *396*, 305–315. [\[CrossRef\]](#)
36. Li, J.; Zhou, F.; Yang, D.; Yu, B.; Li, Y. Effect of swirling flow on large coal particle pneumatic conveying. *Powder Technol.* **2020**, *362*, 745–758. [\[CrossRef\]](#)
37. Mezhericher, M.; Brosh, T.; Levy, A. Modeling of particle pneumatic conveying using, D.E.M and, D.P.M methods. *Part. Sci. Technol.* **2011**, *29*, 197–208. [\[CrossRef\]](#)
38. Chen, L.; Liu, G. Airflow-Dust Migration Law and Control Technology Under the Simultaneous Operations of Shotcreting and Drilling in Roadways. *Arab. J. Sci. Eng.* **2019**, *44*, 4961–4969. [\[CrossRef\]](#)
39. Jägers, J.; Brömmer, M.; Illana, E.; Wirtz, S.; Scherer, V. DEM-CFD simulation of wood pellet degradation by particle-wall impact during pneumatic conveying. *Powder Technol.* **2021**, *391*, 385–402. [\[CrossRef\]](#)
40. Uzi, A.; Levy, A. Flow characteristics of coarse particles in horizontal hydraulic conveying. *Powder Technol.* **2018**, *326*, 302–321. [\[CrossRef\]](#)
41. Yu, H.; Cheng, W.; Wu, L.; Wang, H.; Xie, Y. Mechanisms of dust diffuse pollution under forced-exhaust ventilation in fully-mechanized excavation faces by, C.F.D-DEM. *Powder Technol.* **2017**, *317*, 31–47. [\[CrossRef\]](#)
42. Ebrahimi, M.; Crapper, M. CFD–DEM simulation of turbulence modulation in horizontal pneumatic conveying. *Particuology* **2017**, *31*, 15–24. [\[CrossRef\]](#)

43. Ma, H.; Zhou, L.; Liu, Z.; Chen, M.; Xia, X.; Zhao, Y. A review of recent development for the, C.F.D-DEM investigations of non-spherical particles. *Powder Technol.* **2022**, *412*, 117972. [[CrossRef](#)]
44. Archard, J.F. Contact and Rubbing of Flat Surfaces. *J. Appl. Phys.* **1953**, *24*, 981–988. [[CrossRef](#)]

**Disclaimer/Publisher's Note:** The statements, opinions and data contained in all publications are solely those of the individual author(s) and contributor(s) and not of MDPI and/or the editor(s). MDPI and/or the editor(s) disclaim responsibility for any injury to people or property resulting from any ideas, methods, instructions or products referred to in the content.